

Nanoporous polymeric membranes with tunable 10-nm pore sizes for fast Li⁺ ion mobility and enhanced cyclability in lithium metal batteries

Taeseok Oh^{a,1}, Rak Hyeon Choi^{a,1}, Hye Ryung Byon^{a,b,*}, Myungeun Seo^{a,b,*}

^a Department of Chemistry, Korea Advanced Institute of Science and Technology (KAIST), Daejeon 34141, South Korea

^b KAIST Institute for Nanocentury, KAIST, Daejeon 34141, South Korea

ARTICLE INFO

Keywords:

Nanoporous polymer
3D porous channel
Ion transport
Ion mobility
Lithium-metal batteries

ABSTRACT

Despite extensive studies on nanoporous membranes for regulating lithium-ion (Li⁺) flux in lithium (Li)-metal batteries, the pore size design has largely focused on very small (< 5 nm) or extremely large (> 20 nm) dimensions, overlooking the intermediate pore size range. This gap, particularly between 5 and 15 nm, has limited exploration of critical Li⁺ transport phenomena and their impact on improving cell performance. Here, we developed robust and free-standing polymeric films with three-dimensional (3D) continuous nanoporous channels, precisely tuned to pore diameters ranging from 5 to 14 nm and immobilized sulfonate groups. Our systematic investigations revealed how pore size and immobilized anionic groups correlated with Li⁺ conductivity and battery performance. Notably, sulfonate-functionalized channels promoted Li⁺ conductivity significantly within this optimal pore range compared to non-functionalized counterparts. In an ether-based electrolyte with 1 M lithium bis(fluorosulfonyl)imide (LiFSI), the Li⁺ conductivity peaked at a pore diameter of 10 nm. Furthermore, the mobility of Li⁺ was approximately 4.4 times faster than FSI⁻, resulting in reducing interfacial resistance and promoting uniform Li deposition. The sulfonated nanoporous membrane in Li|LiFePO₄ full cells with an N/P ratio of 2.3 delivered excellent cycling stability over 1000 cycles while retaining approximately 80 % of the initial capacity.

1. Introduction

Lithium (Li)-metal batteries have shown great promise in enhancing energy density by utilizing metallic Li electrodes [1–3]. However, the irregular Li deposition and stripping processes remain major challenges, often leading to dendritic Li growth and the accumulation of solid electrolyte interphase (SEI) layers containing inactive Li [4–7]. These issues persist during charge and discharge cycles, ultimately resulting in poor cycling stability and an increased risk of thermal runaway and fire [5,8–13]. A critical strategy to address these challenges involves regulating Li⁺ flux to achieve uniform Li deposition while minimizing the formation of sacrificial SEI components.

Numerous approaches to controlling Li deposition have been guided by the Sand's time equation (Eq. 1) [14]:

$$t_{\text{sand}} = \pi D \frac{(z_c c_0 F)^2}{4(J t_-)^2} \quad (1)$$

where D is the diffusion coefficient, z_c is the charge number of the cation (1 for Li⁺), c_0 is the bulk salt concentration, F is the Faraday's constant, J is the current density, and t_- is the transference number of anions. Under strict test conditions defined by specific J and c_0 , the key parameter available to extend the Sand's time is t_- . Prolonging the Sand's time delays the onset of the dendrite formation, thereby improving the uniformity of Li deposition.

One strategy has focused on designing membranes with ultra-small sub-nanometer pores to selectively enhance Li⁺ conduction while reducing the transport of larger-size anions, which effectively decreases t_- [15–20]. However, these membranes often face limitations, including reduced ion throughput and increased resistance. The discrete porous channels between porous materials have resulted in inconsistent Li⁺ pathways. The thick deposition of porous materials has also increased overall cell resistance [15–18].

Alternatively, controllable larger sizes and continuous pore channels can provide well-defined ion pathways and reduced ion transport

* Corresponding authors.

E-mail addresses: hbyon@kaist.ac.kr (H.R. Byon), seomyungeun@kaist.ac.kr (M. Seo).

¹ These authors contributed equally to this work.

resistance. Immobilized anionic functional groups that pair with Li^+ ions decrease t_- , while increasing the Li^+ transference number ($t_{\text{Li}^+} = 1 - t_-$). High t_{Li^+} can suppress the anionic concentration polarization during the charge/discharge process, causing low internal impedance and high discharge voltage [21,22]. Anion immobilization is one method of inducing lithium ions to be uniformly distributed and deposited near the lithium metal anode, enabling stable lithium stripping. Increasing t_{Li^+} by using non-coordinating diluents like 1,2-difluorobenzene and maintaining localized high-concentration solvation structures has been shown to enhance interfacial ion transport and suppress dendritic lithium growth, thereby improving battery stability and efficiency [23–25]. Covalent organic frameworks (COFs) with immobilized ionic groups have been introduced to demonstrate this concept [26–29]. However, the limited pore sizes of COFs (2 ~ 5 nm) constrain Li^+ transport behaviors and limit their optimization for electrochemical cell performance within this size range. In comparison, materials with far larger pores and continuous pore channels (e.g., polymer or anodized aluminum oxide membranes with pores exceeding 20 or 70 nm, respectively) have been explored [30–32]. Despite offering low transport resistance, these larger pores lack sufficient selectivity for Li^+ , reducing overall Li^+ transport efficiency.

A significant knowledge gap remains in materials with intermediate pore sizes (e.g., 3 ~ 20 nm), which could offer a better balance between ion selectivity and ion transport resistance. Addressing this gap would enable a more systematic investigation of Li^+ transport dynamics under confined conditions and facilitate the evaluation of their effects on key performance parameters, including ionic conductivity, interfacial stability, and cycling longevity in Li-metal batteries.

To address this gap and unlock new opportunities for enhancing Li-

metal cell performance, we developed Li^+ -conducting nanoporous polymeric membranes with finely tuned pore sizes ranging from 5 to 14 nm. The pore size control was achieved using a block polymer-based method combined with *in situ* polymerization-induced microphase separation (PIMS) [33–36]. The densely crosslinked polymer matrix provided robust and mechanically stable membranes, firmly supporting the formation of three-dimensional (3D)-continuous nanoporous channels. To further enhance selective ion transport, sulfonate groups were immobilized onto the pore channel surfaces, facilitating the accommodation of mobile Li^+ . For studying Li^+ flux, lithium bis(fluorosulfonyl) imide (LiFSI) dissolved in 1,2-diethoxyethane (DEE) electrolyte solution was used as the electrolyte solution. Ion conductivity exhibited a linear increase in pore diameter, reaching a maximum of 0.86 mS cm^{-1} at room temperature for 10 nm pores. Further, the mobility of Li^+ was approximately 4.4 times faster than FSI^- in the sulfonated nanochannels, promoting a uniform Li^+ flux and even Li deposition. It also minimized the formation of extra SEI species arising from the decomposition of FSI^- and DEE. These results led to superior performance in $\text{Li}|\text{LiFePO}_4$ cells over 1000 cycles with the sulfonated nanoporous membranes compared to non-sulfonated ones and commercial Celgard membranes.

2. Results and discussion

Fig. 1a depicts a synthetic route to the functional nanoporous polymer membranes via PIMS. According to the PIMS protocol previously reported elsewhere [1,37,38], a macroporous polyethylene matte is entirely wet with a polymerization mixture composed of polylactide macro-chain transfer agent (PLA-CTA), styrene (S), and divinylbenzene (DVB) as the vinyl monomer and the cross-linker, and

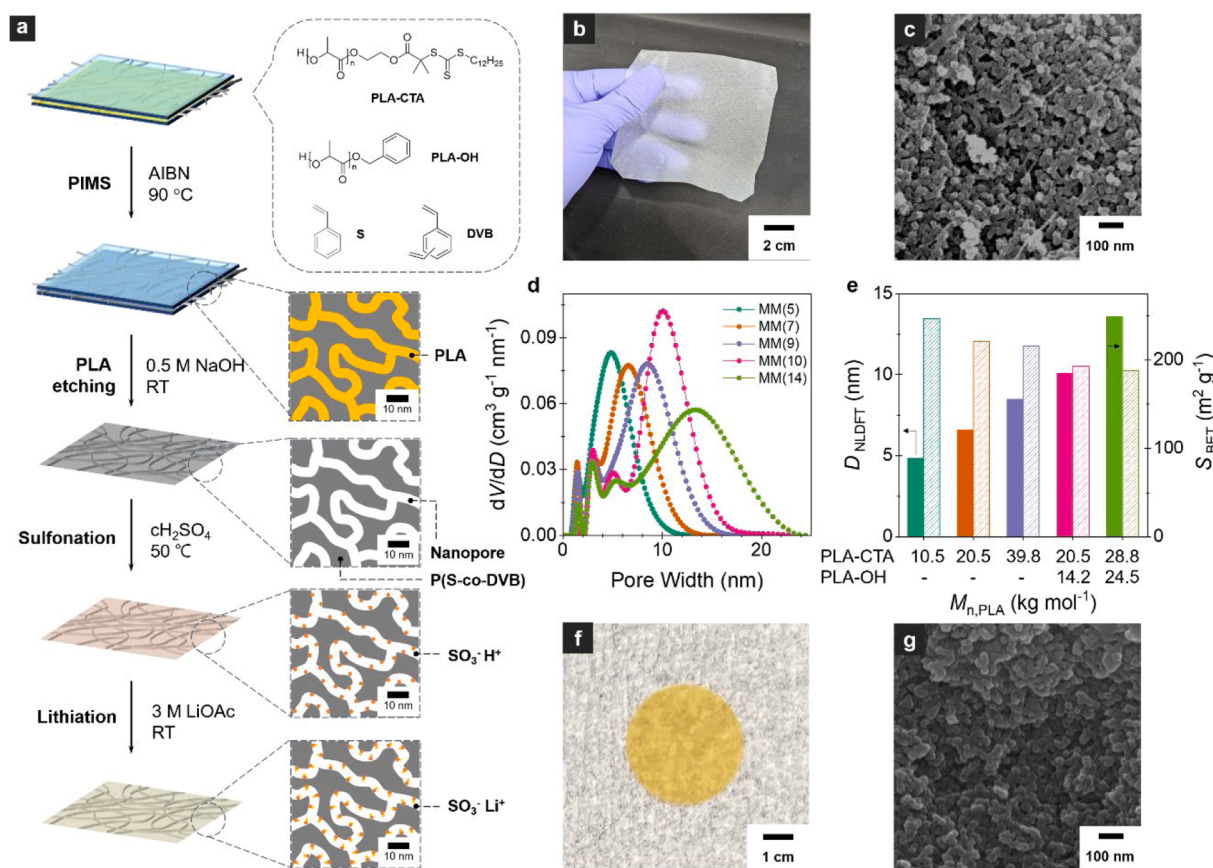


Fig. 1. SMM fabrication. (a) Schematic depiction for the fabrication process. (b) Photo of MM(10). (c) SEM image of MM(10). The sample was coated with osmium prior to imaging. (d) NLDFT pore size distributions of MM obtained by the nitrogen sorption isotherm analysis at 77 K. The adsorption branch was used for the analysis. (e) Mode pore size (from d) and S_{BET} values of MMs synthesized in this study. For MM(10) and MM(14), the PLA weight composition was PLA-CTA:PLA-OH = 4:6. (f) Photo of SMM(10). (g) SEM image of SMM(10).

azobisisobutyronitrile (AIBN) as the thermal radical initiator, and then sandwiched between two glass plates [33]. PLA-CTA, with an excessively large molecular weight, increases the viscosity of the polymerization mixture, making it difficult to synthesize a uniform membrane. Thus, hydroxyl-terminated PLA (PLA-OH) is added to increase the pore size for synthesizing membranes with pores larger than 10 nm [39]. Heating the assembly to 90 °C initiates controlled radical copolymerization of S and DVB via the reversible addition-fragmentation chain transfer (RAFT) mechanism mediated by the CTA motif at the PLA chain end. The increasing incompatibility of PLA to the forming P(S-co-DVB) block, growing from the PLA terminus, spontaneously induces microphase separation into a disordered bicontinuous morphology of PLA and P(S-co-DVB) domains. The polymerization proceeds to nearly complete conversion while the bicontinuous morphology arrested by *in situ* cross-linking with DVB persists. Immersing the assembly in the basic solution detaches the membrane from glass and also etches PLA to produce nanopores supported by the cross-linked polystyrenic framework. We typically fabricate membranes of 10 cm × 10 cm × 25 μm (thickness, *t*) dimensions with reliable thickness control (Fig. 1b). A representative scanning electron microscopy (SEM) image visualizes the characteristic 3D continuous nanopores produced by the PIMS process (Fig. 1c).

The crucial feature of the PIMS approach is the straightforward control over the pore size as the PLA domain templates the void. By varying the number-average molar mass (M_n) of PLA-CTA from 10.5, 20.5, and 39.8 kg mol⁻¹ (see the Supporting Information, Table S1 and Fig. S1-S2 for the synthetic details), nanoporous membranes with mode pore size of 5, 6, and 9 nm were successfully produced as estimated by nonlocal density functional theory (NLDFT) analysis of the nitrogen sorption isotherm data (Figs. 1d and S3). Membranes possessing larger pores of 10 and 14 nm were obtained by adding PLA-OH into the polymerization mixture to swell the resulting PLA domain [34]. Importantly, as we kept the total PLA weight fraction to 40% in the polymerization mixture to maintain a large pore volume, the specific surface area estimated by Brunauer-Emmett-Teller analysis (S_{BET}) decreased with the increasing pore size. Fig. 1e summarizes the mode pore size and S_{BET} of the membranes synthesized. SEM and small angle X-ray scattering (SAXS) analyses also supported successful pore size control while retaining the 3D continuous pore structure, facilitating transport without domain alignment (Figs. S4-S5). As the pore size range falls into the mesoporous regime, we denote the synthesized mesoporous

membranes as MM(*x*), where *x* represents the mode pore diameter (D_{NLDFT}). Table 1 summarizes the characterization details of MMs synthesized in this study.

To ensure thermal and mechanical strength, the cross-linking density of MMs was regulated by using 60 mol% DVB. This formulation retained both pore structure and specific surface area at 100 °C, in contrast to the pore deformation with 20 mol% DVB in SAXS analysis. This result indicated superior resistance of cross-linked MM to collapse under Laplace pressure (Fig. S6) [1,40,41]. Following solvent uptake with acetonitrile (MeCN) or DEE, the MMs exhibited excellent structural stability, as evidenced by consistent scattering features in SAXS patterns (Fig. S7). Interestingly, when exposed to a mixture of 1,3-dioxolane/1,2-dimethoxyethane (DOL/DME) or ethyl carbonate/diethyl carbonate (EC/DEC), the MMs showed SAXS signal broadening and attenuation, suggesting significant swelling and deformation of the polystyrenic framework, respectively.

In addition to MMs, we developed an anionic sulfonate group-immobilized variant, indicated as SMM. The MMs were immersed in concentrated sulfuric acid for varying reaction times, with an optimal duration of 36 h. Sulfonic acid (-SO₃H) groups were immobilized on the porous walls via electrophilic aromatic substitution. Following sulfonation, the H⁺ ions from the sulfonic acid groups were exchanged with Li⁺ by treatment with excess lithium acetate solution, a process referred to as lithiation (Fig. 1f). The sulfonated and lithiated MMs are denoted as SMM(*x*)_{H+} and SMM(*x*)_{Li+}, respectively. In tensile testing, MM(10) (760 MPa) and SMM(10)_{Li+} (821 MPa) showed Young's moduli similar to Celgard2500 (808 MPa) (Fig. S8). Lower elongations at break than Celgard2500 seem to originate from the densely cross-linked polystyrenic framework, which is essential to withstand the nanoporous structure consisting of <15 nm pores. We note that the modulus and elongation can be adjusted by controlling cross-linking density [38].

The density of immobilized sulfonic acid substituents was estimated from the elemental sulfur content, representing the theoretical ion exchange capacity (IEC_{theo}). This estimate was further validated by back-titration of the H⁺ concentration, yielding the calculated IEC (IEC_{calc}) (Table 1, see details in Experimental Section in SI). Both IEC_{theo} and IEC_{calc} decreased with increasing pore diameters of the polystyrenic framework. After lithiation, the concentration of Li⁺ associated with immobilized sulfonate groups ([Li⁺]_{SO3-}) was quantified. As the pore diameter increased, [Li⁺]_{SO3-} concentrations decreased from 1.6 to 1.0 mmol g⁻¹ (Table 1), aligning with the observed decreasing IEC values. It confirmed the successful ion exchange from H⁺ to Li⁺ on the sulfonate groups. Notably, the sulfonation and lithiation processes did not alter the structural integrity of polystyrenic frameworks or pore structures. SEM and SAXS analyses confirmed the preservation of framework morphology and pore sizes relative to the parent MMs (Fig. S9-S10). Fourier transform infrared (FTIR) spectra verified the chemical stability after these treatments (Fig. S11). The solvent-dependent stability of SMMs also followed a similar pattern to that of MMs, as evidenced by SAXS analysis (Fig. S12).

To assess the ionic conductivity (σ) of MMs and SMM_{Li+}s (*t* = 25 μm) as nanoporous membranes, a 1 M LiFSI in DEE (60 μL, σ = 9.88 mS cm⁻¹ at 25 °C) was injected and allowed to incubate for 12 h before all electrochemical tests. The transport of Li⁺ and FSI⁻ ions through the porous 3D channels was influenced by the pore size and the concentration of the sulfonate groups, which governed the σ value. We observed different trends in σ for MMs and SMM_{Li+}s relative to pore size. MMs exhibited a linear increase in σ with increasing pore diameters in 5 – 14 nm (Figs. 2a and S13, and Tables 1 and S2). The maximum σ of MM (14), 0.69 mS cm⁻¹, was more than 5.5 times higher than the one of MM (5). This result demonstrates the significant resistance introduced by smaller pore diameters. Interestingly, the σ of MM(14) was higher than that of the commercial membrane, Celgard2500 (0.58 mS cm⁻¹ with 55% porosity, Fig. S13a), which features pores in the hundreds of nanometers but the same thickness. It suggests that a pore diameter of 14 nm facilitates ion transport more than the large pores in

Table 1
Characteristics of MMs and SMMs.

		Mode pore diameter (nm)				
		5	6	9	10	14
MM	D_{NLDFT} (nm) ^a	4.8	6.1	9.1	10.1	13.6
	V (cm ³ g ⁻¹) ^b	0.360	0.406	0.486	0.561	0.580
	S_{BET} (m ² g ⁻¹) ^c	247	221	216	193	188
	σ (mS cm ⁻¹) ^d	0.12	0.17	0.35	0.48	0.69
SMM _{H+} ^e	IEC _{theo} (mmol g ⁻¹) ^f	1.968	1.943	1.949	1.920	1.840
	IEC _{calc} (mmol g ⁻¹) ^g	1.347	1.162	1.190	1.025	0.958
	[Li ⁺] _{SO3-} (mmol g ⁻¹) ^h	1.590	1.542	1.464	1.374	1.004
SMM _{Li+} ^e	(mmol g ⁻¹) ^h	(0.009)	(0.015)	(0.018)	(0.028)	(0.042)
	σ (mS cm ⁻¹) ^d	0.15	0.43	0.64	0.84	0.77

a Estimated from the adsorption branch; b Pore volume calculated from the point $P/P_0 = 0.95$; c Measured by multipoint BET analysis at $P/P_0 = 0.2 - 0.35$; d Measured by electrochemical impedance spectroscopy (EIS) at 25 °C; e Sulfonation for 36 h; f Estimated from the elemental analysis of sulfur content; g Measured by back-titration using NaOH; h Average Li⁺ concentrations from SMM_{Li+}, measured by inductively coupled plasma-optical emission spectroscopy (ICP-OES) after extraction of Li⁺ into an acidic solution. The parenthesis indicates the standard deviations derived from three independent measurements.

Celgard2500.

We synthesized SMM(10)s by varying the weight fraction of PLA (w_{PLA}) as the sacrificial block to investigate the porosity effect. Based on the nitrogen sorption isotherm analysis (Fig. S14), the pore volume of the synthesized MM(10)s increased from 0.25 to 0.50 $\text{cm}^3 \text{g}^{-1}$ with the increasing w_{PLA} from 0.2 to 0.4 (Table S3). Preparing a polymerization mixture with w_{PLA} higher than 0.4 was challenging because of the high viscosity. In the SMM(10) $_{\text{Li}^+}$ state, we observed an increase in the ionic conductivity with the increasing porosity, presumably because of the larger uptake of the liquid electrolyte solution in the pore and the higher number of SO_3Li groups on the pore surface. We also optimized the SMM(10) $_{\text{Li}^+}$ thickness to maximize the ionic conductivity. By reducing t from 145 to 25 μm , the ionic conductivity increased from 0.66 to 0.85 mS cm^{-1} , consistent with the decrease in resistance (Table S4). We note that 25 μm is comparable to the thickness of conventional polymer separators such as Celgard2500 (25 μm thick).

Under similar conditions, SMM $_{\text{Li}^+}$ showed a volcano-shaped conductivity trend (Fig. 2a). The σ sharply increased with pore size, peaking at 0.84 mS cm^{-1} for SMM(10) $_{\text{Li}^+}$, which surpassed the performance of MM(14). Beyond a pore size of 10 nm, σ declined to 0.72 mS cm^{-1} for SMM(14) $_{\text{Li}^+}$. It is likely due to a substantial reduction in $[\text{Li}^+]_{\text{SO}_3^-}$ concentrations compared to the more gentle decrease in smaller pore sizes. Notably, despite SMM(5) $_{\text{Li}^+}$ having the highest $[\text{Li}^+]_{\text{SO}_3^-}$ concentration, its lowest σ explained significant ion-transport resistance caused by the excessively narrow pore size. Therefore, the superior σ for SMM(10) $_{\text{Li}^+}$ arises from an optimal balance between pore size and sulfonate group concentration.

The influence of $[\text{Li}^+]_{\text{SO}_3^-}$ concentration was further investigated at a constant pore size. Sulfonation reaction times were adjusted from 12 to 36 h, resulting in $[\text{Li}^+]_{\text{SO}_3^-}$ concentrations ranging from 1.19 to 1.37

mmol g^{-1} in SMM(10) $_{\text{Li}^+}$ (Fig. 2b and Table 2). After 36 h of reaction, the $[\text{Li}^+]_{\text{SO}_3^-}$ concentration reached saturation, enabling SMM(10) $_{\text{Li}^+}$ to accommodate approximately 40 mol% of Li^+ from a 1 M LiFSI solution and yielding a total Li^+ concentration of 1.4 M (Fig. 2 and Fig. S15). Correspondingly, σ increased from 0.62 to 0.86 mS cm^{-1} , respectively, demonstrating that increasing $[\text{Li}^+]_{\text{SO}_3^-}$ concentrations enhances σ .

Furthermore, the Li^+ transference number (t_{Li^+}) provides insight into the advantage of immobilized sulfonate groups regarding Li^+ mobility. In contrast to MM(10) and the Celgard2500, which exhibit t_{Li^+} values of 0.49 and 0.42, respectively (Fig. S16), the t_{Li^+} values for SMM(10) $_{\text{Li}^+}$ increased from 0.62 to 0.86 with prolonged sulfonation times (Fig. 2b and Table 2). This trend reveals that Li^+ mobility is approximately 4.4 times faster than that of FSI^- for SMM(10) $_{\text{Li}^+}$ after 36 h of sulfonation, in contrast to their similar velocities in MM(10), as described by Eq. (2) [42]:

Table 2

Sulfonation-time dependency of electrochemical characteristics of SMM(10) $_{\text{Li}^+}$. $[\text{Li}^+]_{\text{SO}_3^-}$, t_{Li^+} , σ , σ_{Li^+} , E_a indicate the concentration of Li^+ pairing with immobilized sulfonate groups, Li^+ transference number, ionic conductivity, Li^+ conductivity, and activation energy. The (sat) indicates the saturated concentration.

Sulfonation time of SMM(10) $_{\text{Li}^+}$	12 h	24 h	36 h
$[\text{Li}^+]_{\text{SO}_3^-}$ (mmol g^{-1})	1.186	1.246	1.368 (sat)
t_{Li^+}	0.62	0.71	0.86
σ (mS cm^{-1})	0.52	0.63	0.83
σ_{Li^+} (mS cm^{-1})	0.32	0.45	0.72
E_a (eV)	0.13	0.12	0.06

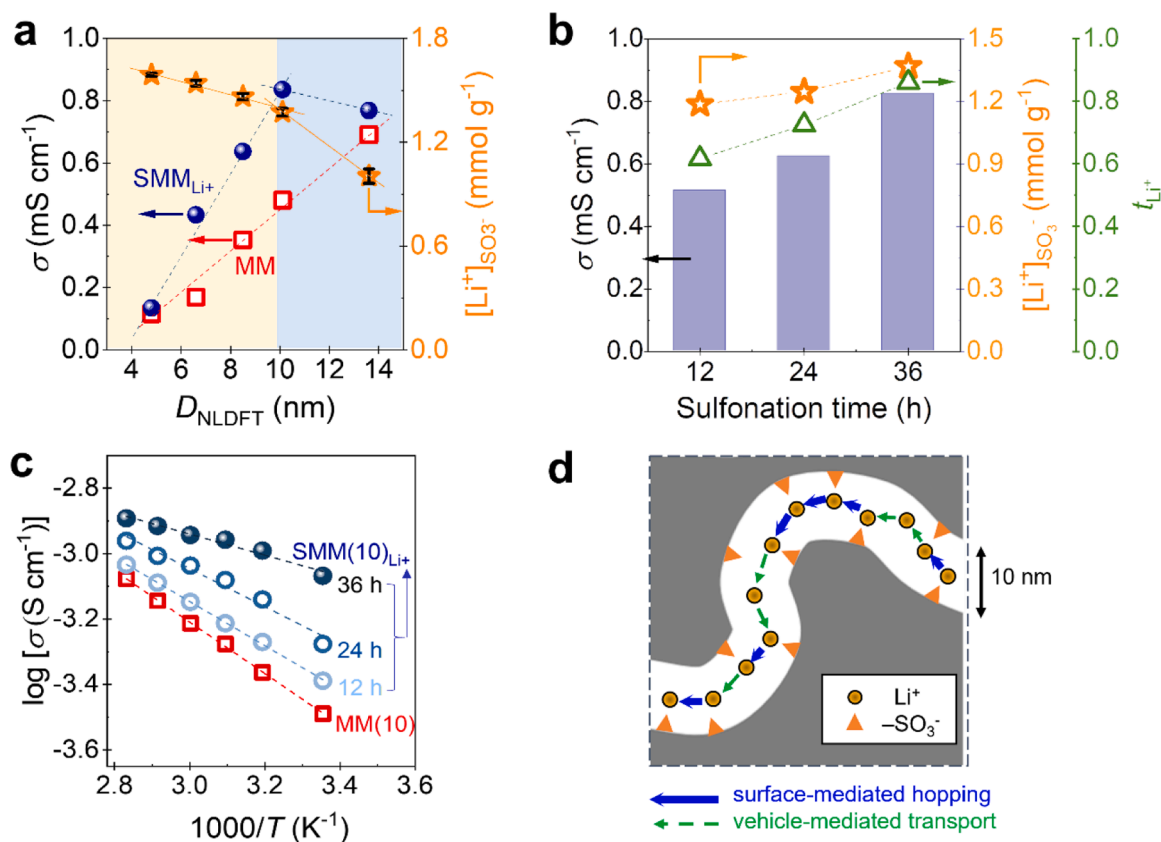


Fig. 2. Electrochemical characterizations of MM and SMM membranes ($t = 25 \mu\text{m}$) with 1 M LiFSI/DEE electrolyte solution. All tests were examined at room temperature except (c). (a) Ionic conductivity (σ) of MM and SMM $_{\text{Li}^+}$ as a function of pore size (D_{NLDFT}) and corresponding the concentration of $[\text{Li}^+]_{\text{SO}_3^-}$. (b) Correlation between sulfonation time of SMM(10) $_{\text{Li}^+}$ and electrochemical parameters. (c) Arrhenius plots of MM(10) and SMM(10) $_{\text{Li}^+}$ with different sulfonation durations. (d) Proposed schematic illustration of Li^+ transport behavior in SMM(10) $_{\text{Li}^+}$. FSI $^-$ and DEE are omitted for clarity.

$$t_{Li+} = \frac{F(c_{0,+} + \nu_+ |z_+|)}{F[(c_{0,+} + \nu_+ |z_+|) + (c_{0,-} - \nu_- |z_-|)]} \quad (2)$$

where F is Faraday's constant, c_0 is the bulk ion concentration (with 0.4 M $[Li^+]_{SO_3}$ added to 1 M Li^+ for SMM(10) $_{Li+}$), ν is the ion mobility, and z is the charge number of the cation (1 for Li^+). The subscripts $+$ and $-$ indicate Li^+ and FSI $^-$ ions, respectively. The presence of immobilized sulfonate groups on the porous walls pronouncedly enhances Li^+ mobility, boosting ion conductivity and promoting uniform Li^+ flux. As a result, the estimated Li^+ conductivity (σ_{Li+}), calculated by multiplying σ and t_{Li+} , reached 0.72 mS cm $^{-1}$ for SMM(10) $_{Li+}$ (Table 2). It was more than 3 times higher than that of MM(10) and Celgard2500, both of which had σ_{Li+} values of approximately 0.24 mS cm $^{-1}$. The contribution of mobile Li^+ paired with sulfonate groups was also validated by comparing non-lithiated SMM(10) $_{H+}$ with the constant t_{Li+} of 0.49 regardless of sulfonation durations (Fig. S17 and Table S5). It was due to the immobile H^+ ions in the sulfonic acid groups, resulting in non-ion-selective transport.

Arrhenius plots in Fig. 2c revealed the activation energy (E_a) barrier for ion transport in both MM(10) and SMM(10) $_{Li+}$. The estimated E_a values were 0.16, 0.13, 0.12, and 0.06 eV for MM(10) and SMM(10) $_{Li+}$ subjected to 12, 24, and 36 h of sulfonation, measured within the temperature range of 25–80 °C. In MM(10), ion transport predominantly follows a vehicle-like mechanism through the pores [36], characteristic of electrolyte dynamics in the liquid solution. In contrast, Li^+ transport in SMM(10) $_{Li+}$ appears more complex, involving a combination of vehicle-like transport and hopping through sulfonate sites on the pore surface. Nonetheless, the decrease in E_a with increasing $[Li^+]_{SO_3}$ concentration underpins the importance of surface-mediated Li^+ transport, which significantly enhances Li^+ mobility (Fig. 2d). Conversely, the anionic sulfonate groups impede FSI $^-$ mobility due to electrostatic repulsive interactions, reducing its contribution to the overall ion conductivity.

Utilizing SMM(10) $_{Li+}$ and MM(10) as the nanoporous membranes in Li|Li symmetric cells, interfacial resistances ($R_{interfacial}$) were measured at 25 °C (Fig. 3a). EIS measurements were conducted at open circuit voltage (OCV) after injecting 60 μ L of 1 M LiFSI in DEE solution and resting for 12 h. A stable interface between Li and the membrane was observed with SMM(10) $_{Li+}$. The $R_{interfacial}$ of SMM(10) $_{Li+}$ decreased with increasing sulfonation times (Fig. S18). SMM(10) $_{Li+}$ with 36 h of sulfonation exhibited an $R_{interfacial}$ of 60.2 Ω cm $^{-2}$, approximately half that of MM(10) (140.8 Ω cm $^{-2}$) and significantly lower than Celgard2500 (102.1 Ω cm $^{-2}$) (Table 3). The higher $R_{interfacial}$ for MM(10) compared to Celgard2500 suggests the presence of pronounced membrane resistance in the absence of $[Li^+]_{SO_3}$.

Fig. 3b shows galvanostatic profiles of the Li symmetric cells during the Li plating and stripping processes. SMM(10) $_{Li+}$ exhibited a lower initial Li nucleation potential of approximately 40 mV compared to MM(10) and Celgard2500, which required 70 and 140 mV, respectively, at a current density of 1 mA cm $^{-2}$ and a capacity of 1 mAh cm $^{-2}$ (Fig. 3c). This voltage hysteresis trend was consistent with the Tafel plots (Fig. S19). The exchange current density (j_0) was 6.5×10^{-4} mA cm $^{-2}$ for SMM(10) $_{Li+}$ and 2.7×10^{-4} mA cm $^{-2}$ for MM(10), confirming the faster charge-transfer rate with SMM(10) $_{Li+}$.

In continuous galvanostatic cycling, MM(10) showed an increased voltage hysteresis of approximately 100 mV for 500 h, ultimately leading to cell failure within 700 h (Fig. 3d–e). This performance was superior to Celgard2500, which showed a voltage hysteresis increase to a maximum of 203 mV over 200 h, causing cell failure within 500 h. Despite their similar σ (0.5–0.6 mS cm $^{-1}$) and t_{Li+} (<0.5), the improved cyclability with MM(10) is presumably due to more uniform Li^+ flux through its nanoporous channels [43]. SEM images of Li surfaces with these membranes corroborated this hypothesis, showing a more uniform surface with MM(10) (Fig. 3 and Fig. S20). In comparison, SMM(10) $_{Li+}$ substantially outperformed both MM(10) and Celgard2500. Stable

voltage hysteresis of approximately 20 mV was maintained for up to 2000 h (Fig. 3d–e). The average Coulombic efficiencies (CEs) during 200 cycles were 98.91% for SMM(10) $_{Li+}$, higher than 98.53% for MM(10) and 80.35% (by 100 cycles) for Celgard2500 (Fig. 3f and Fig. S21), in line with their respective cyclability results. This excellent cyclability with SMM(10) $_{Li+}$ is attributed to its notably high σ and low $R_{interfacial}$. In addition, predominant and fast Li^+ transport through the sulfonate groups ensures a more uniform and consistent Li^+ flux. SEM images of the Li surface in Fig. 3i revealed the granular shape and even Li surface morphology after 20 cycles with SMM(10) $_{Li+}$. Further, rate capability was examined at increasing current densities from 2 to 20 mA cm $^{-2}$ while maintaining a capacity of 2 mAh cm $^{-2}$ (Fig. S22). Compared to the use of a Celgard2500, the Li symmetric cell assembled with SMM(10) $_{Li+}$ exhibited significantly lower voltage hysteresis, particularly at higher current densities. At 2 mA cm $^{-2}$, the voltage hysteresis values were 51.6 mV and 42.2 mV for Celgard2500 and SMM(10) $_{Li+}$, respectively. This gap widened at 10 mA cm $^{-2}$, with hysteresis increasing to 191.4 mV for Celgard2500, while remaining at only 77.6 mV for SMM(10) $_{Li+}$. Notably, the SMM(10) $_{Li+}$ cell maintained stable operation even at a high current density of 20 mA cm $^{-2}$, whereas the Celgard2500 cell failed beyond 12 mA cm $^{-2}$. In addition, the SMM(10) $_{Li+}$ cell was cycled over 110 h at a current density of 5 mA cm $^{-2}$ and a capacity of 5 mAh cm $^{-2}$ with reasonably low voltage hysteresis of 28.5 mV (Fig. S23). In contrast, the Celgard2500 and MM(10) cells failed within 30 h and 70 h, respectively.

X-ray photoelectron spectroscopy (XPS) analysis revealed chemical composites of the SEI layer after 20 cycles at 1 mA cm $^{-2}$ and 1 mAh cm $^{-2}$ condition. With MM(10), F, S, and N species (15.5 % in total) and carbon (23 %) were predominant on the delaminated SEI layers (Fig. 3h). In the F 1s, N 1s, and S 2p binding energy (BE) regions, the presence of LiF, Li $_3$ N, LiN $_x$ O $_y$, Li $_2$ S, and SO $_3$ /SO $_x$ species was attributed to the decomposition of FSI $^-$ (Fig. 3k and Fig. S24). Also, intense C–O signals in the C 1s and O 1s BE regions originated from the decomposition of the DEE solvent. After Ar $^+$ etching for 360 s, the carbon contents decreased considerably to 2.8%, indicating that an organic layer covered the underlying inorganic species. This laminated SEI formation hindered uniform Li^+ flux on the Li electrodes, leading to irregular Li deposition and thicker SEI layers. It caused increased voltage hysteresis and rapid cell failure. In sharp contrast, when SMM(10) $_{Li+}$ was used, the Li electrode surface primarily consisted of Li and O, forming Li $_2$ O and Li $_2$ CO $_3$. The atomic % of F, S, and N species was minimal (<2.5% combined), and the carbon content was also low (12.7%, reduced to 1.8% after Ar $^+$ etching) (Fig. 3j–l and Fig. S24). The negligible presence of FSI $^-$ fragments was supported by low FSI $^-$ transport (Fig. 3l). This result unveiled a dominant and uniform Li^+ flux on the Li electrode with minimal interference from FSI $^-$ and DEE solvents, contributing to prolonged cyclability with stable and low-voltage hysteresis.

For full cell tests, Li|LiFePO $_4$ cells with an N/P ratio of 9 were employed. The stable rate capability was evaluated from 0.1 to 2 C with SMM(10) $_{Li+}$ and MM(10) (Fig. 4a). A capacity gap emerged at the high 2 C rate, delivering 126 mAh g $^{-1}$ for SMM(10) $_{Li+}$ compared to 103 mAh g $^{-1}$ for MM(10) and Celgard2500 (Fig. 4b and Fig. S25). The superior rate capability of SMM(10) $_{Li+}$ was attributed to faster Li^+ mobility and a continuous Li^+ supply by immobilized sulfonate groups. For long-term cycling (500 cycles), SMM(10) $_{Li+}$ retained 99.90 % of its capacity (Fig. 4c), superior to MM(10) (98.0 %) and Celgard2500 (76.0 %) (Fig. 4d). Capacity decay was observed for MM(10) and Celgard2500 after 800 and 500 cycles, respectively (Fig. S26). In contrast, SMM(10) $_{Li+}$ maintained a capacity retention of 93.8 % at 1 C over 1000 cycles. Cross-sectional SEM and SAXS analyses of SMM(10) $_{Li+}$ after 1000 cycles clearly showed that the characteristic nanoporous structure was well preserved, indicating high stability of the membrane during the cell operation condition (Figs. S27 and S28).

When the N/P ratio was reduced to 2.3, the cyclability gap between SMM(10) $_{Li+}$ and MM(10) became more pronounced. Despite their similar initial capacities of around 3.27 mAh cm $^{-2}$, corresponding to

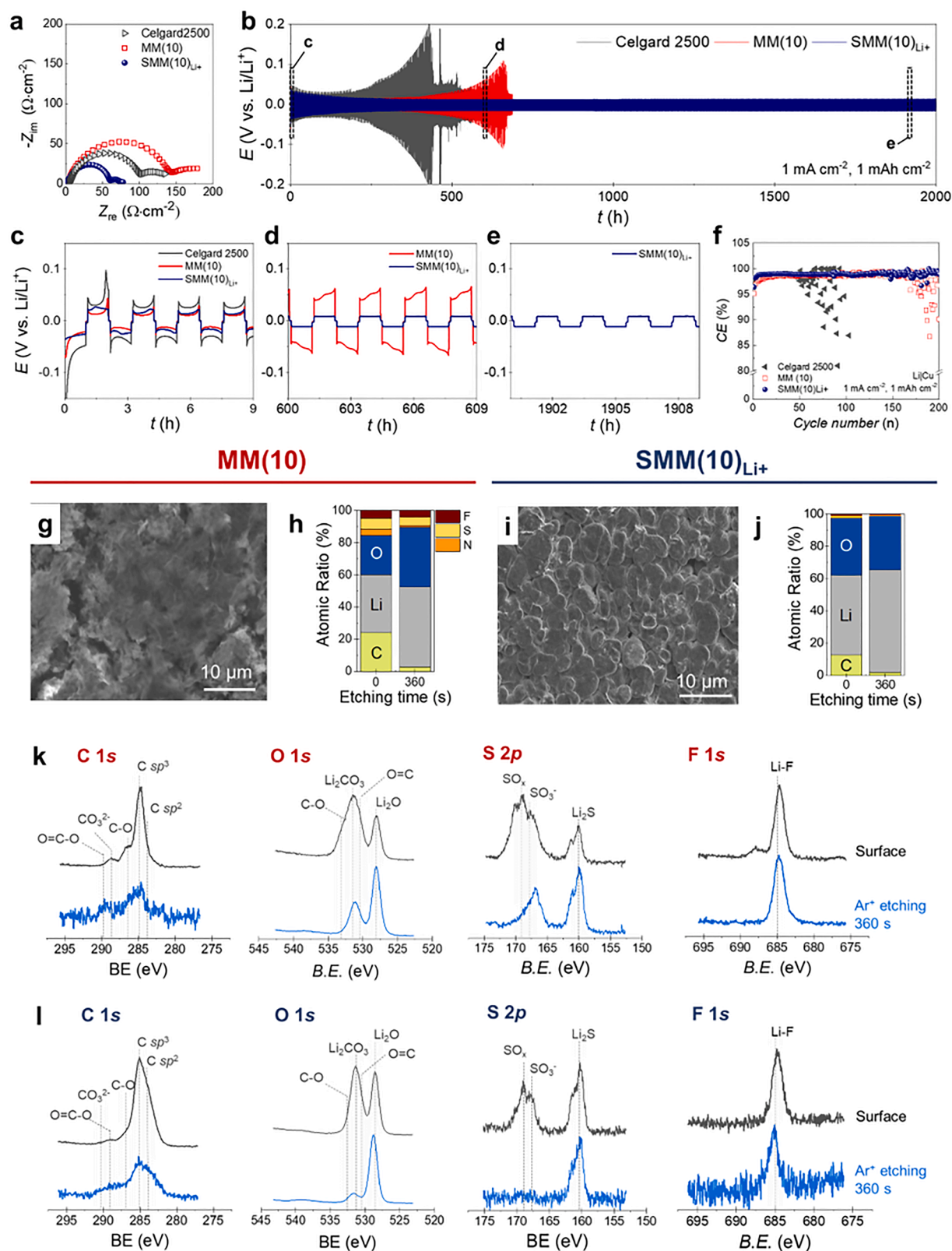


Fig. 3. Li|Li symmetric cell tests with 1 M LiFSI/DEE electrolyte solution at 25°C and analyses. (a) Nyquist plots measured at an amplitude of 10 mV and a frequency range of 1 MHz to 0.1 Hz. (b–e) Galvanostatic cyclability at 1 mA cm^{-2} and 1 mAh cm^{-2} . Voltage profiles were zoomed in (c) at the initial cycle, (d) after 600 h, and (e) after 1900 h. (f) Coulombic efficiency (CE) of Li|Cu cells at 1 mA cm^{-2} , 1 mAh cm^{-2} , and 25°C . (g–l) Post-mortem analysis of Li electrode surface with (g, h, k) MM(10) and (i, j, l) SMM(10)_{Li+} after 20 cycles at 1 mA cm^{-2} and 1 mAh cm^{-2} . (g, i) SEM images of Li surface. (h, j) Atomic percent ratio before and after Ar^+ etching for 360 s. (k–l) XPS spectra at C 1s, O 1s, S 2p, and F 1s binding energy (BE) regions before (black) and after Ar^+ etching (blue).

Table 3Comparative SMM(10)_{Li+}, MM(10), and Celgard2500 in electrochemical tests.

Membranes		Celgard2500	MM (10)	SMM (10) _{Li+} ^a
Li Li cells	$R_{\text{interfacial}}$ ($\Omega \cdot \text{cm}^2$) ^b	102.1	140.8	60.2
	Voltage hysteresis ^c (First cycle, mV)	~140	~70	~40
	Cyclability (h) ^c	~500	~700	~2000
Li Cu cells	CE (%) ^d	97.71	98.16	98.63
Li FePO ₄ cells	Cyclability (times, N/P ~9) ^e	500 ^g	815 ^g	1310 ^g
	Capacity retention (% by 500 cycles, N/P ~9) ^e	76.0	98.0	99.9
	Cyclability (times, N/P ~2.3) ^f	NA	80 ^h	1000 ^g

a 36 h sulfonation; b OCV at 25 °C; c 1 mA cm⁻² and 1 mAh cm⁻²; d 0.5 mA cm⁻² and 1 mAh cm⁻² for 100 cycles; e 1 C at 25 °C; f 0.2 C/0.3 C for charging/discharging at 25 °C; g cyclability by ~80 % capacity retention; h cell failure due to overcharging.

91.6 % of the theoretical capacity (3.57 mAh cm⁻²) at 0.2 C and 0.3 C charging/discharging rates, MM(10) underperformed after 80 cycles (Fig. 4e and Fig. S29). In contrast, SMM(10)_{Li+} sustained 1000 cycles with a capacity retention of 80.2 % and an average CE of 99.999 %. Rate

capability tests from 0.2 to 5 C demonstrated that the discharging capacity gap increased with higher current rates. At 5 C, the measured discharge capacity was 0.976 mAh cm⁻² for SMM(10)_{Li+}, which was superior to Celgard2500 at 0.079 mAh cm⁻² and MM(10) at 0.786 mAh cm⁻² (Fig. S30). At 0.33 C/1 C (charging/discharging) rate, the Li|LFP full cell with SMM(10)_{Li+} performed stably over 100 cycles with an average CE of 99.911 % (Figure S31). In contrast, the Celgard2500 displayed significant overcharge from the 15th cycle (average CE by 14 cycles: 92.87 %), and the MM(10) exhibited similar overcharge behavior from the 39th cycle (CE by 38 cycles: 97.26 %). It underpinned the crucial role of fast and predominant Li⁺ transport through sulfonated and 10 nm diameter 3D nanochannels.

Finally, full cells of Li|Ni_{0.8}Co_{0.1}Mn_{0.1}O₂ (NCM811) using SMM(10)_{Li+} also demonstrated excellent performance. At a 1 C rate for the charging and discharging processes, the presence of SMM(10)_{Li+} resulted in stable 200 cycles with a CE of 99.750 %, whereas the inclusion of Celgard2500 led to cell failure after 40 cycles due to an overcharging issue (Fig. 5). This result demonstrated the feasibility of SMM(10)_{Li+} for high-voltage cathodes.

3. Conclusion

In summary, we systematically explored the influence of nanoporous channels with diameters ranging from 5 to 14 nm in polymeric

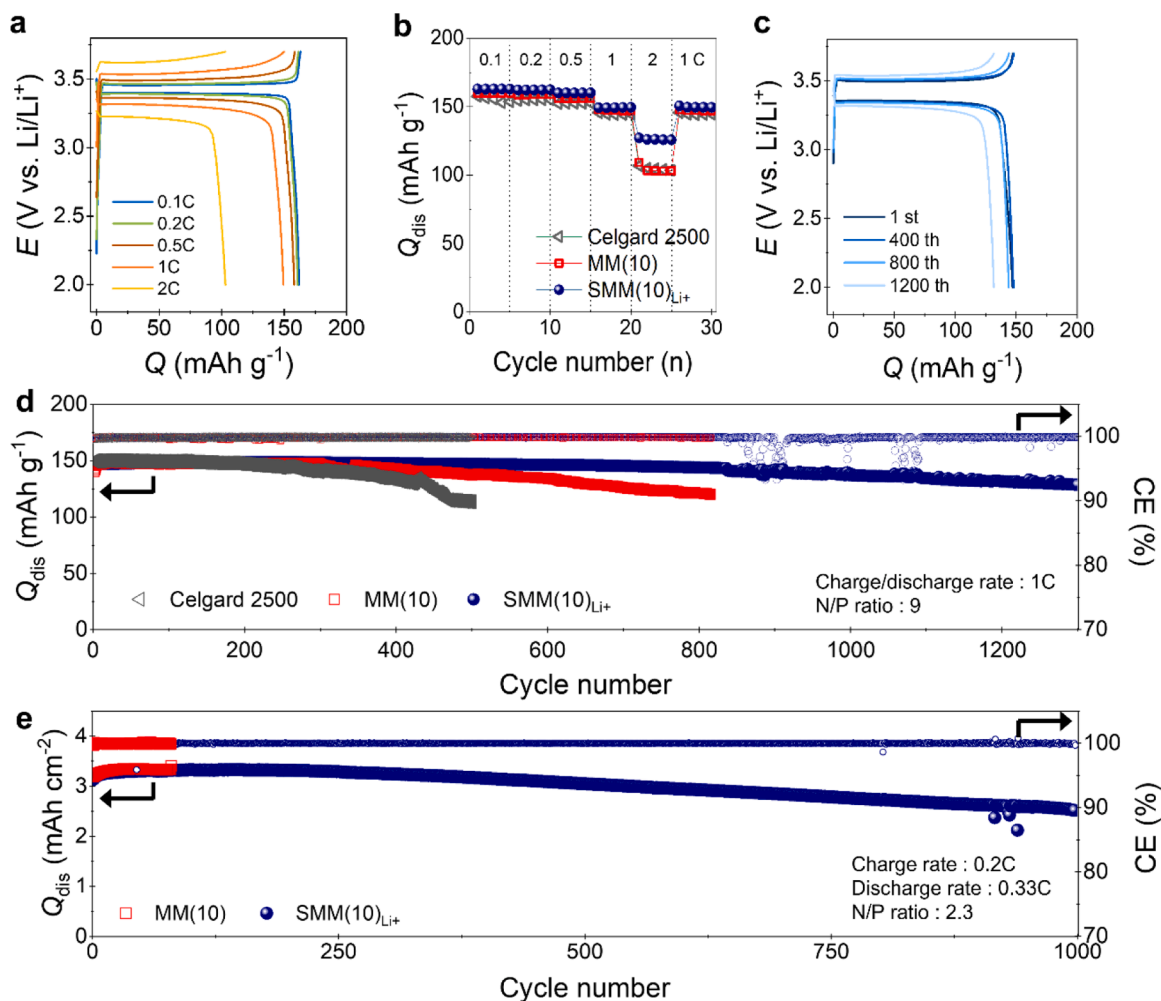


Fig. 4. Electrochemical performance of Li|LiFePO₄ coin cells with 1 M LiFSI/DEE electrolyte solution. N/P ratio was (a-d) 9 and (e) 2.3. (a) Voltage profiles with SMM(10)_{Li+} at different current rates. (b) Comparative rate capability with SMM(10)_{Li+} and MM(10). (c) Cycled voltage profiles with SMM(10)_{Li+} at 1 C. (d) Cyclability with SMM(10)_{Li+}, MM(10), and Celgard2500 at charging and discharging rates of 1 C. (e) Cyclability tests at a charging rate of 0.2 C and a discharge rating of 0.33 C. Q_{dis} and CE indicates discharge capacity and Coulombic Efficiency, respectively.

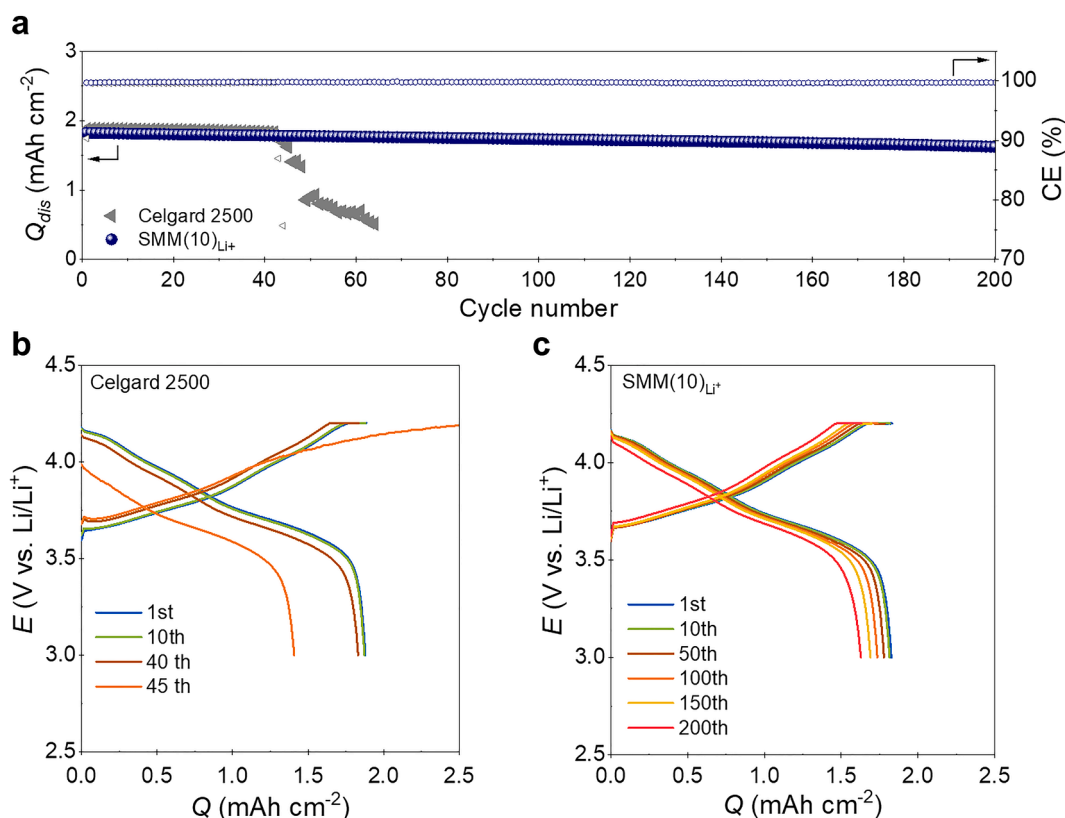


Fig. 5. Full cell tests using Li||NCM811 (capacity = 2 mAh cm^{-2} , N/P ratio = 4) at a charging/discharging rate of 1 C and 25°C . (a) Long-term cycling profiles with SMM(10) Li^+ and Celgard2500 at 25°C . (b–c) Corresponding voltage profiles with (b) Celgard2500, (c) SMM(10) Li^+ .

membranes for Li-metal batteries. By employing a block copolymer-based PIMS methodology, we fabricated $25 \mu\text{m}$ -thick and free-standing membranes featuring continuous, percolating nanopores with precisely controlled diameters. By introducing sulfonate functional groups along the channel walls, systematic studies correlating pore size, Li^+ conductivity, and cell performance rendered insights into Li^+ transport within nanoporous channels. Notably, the optimal ionic conductivity was achieved at a 10 nm pore diameter, attributed to enhanced Li^+ concentration and faster Li^+ mobility facilitated by the immobilized sulfonate groups. These membranes demonstrated excellent cycling stability through uniform Li deposition on the Li electrode while minimizing SEI formation in Li|Li cells. In Li|LiFePO₄ full cells with an N/P ratio of 2.3, they delivered over 1000 cycles with around 80 % capacity retention. This study highlights the critical role of $\sim 10 \text{ nm}$ nano-channels in sulfonate-functionalized polymeric membranes, providing an optimized confined environment for efficient Li^+ transport and improved Li-metal cell performance.

CRediT authorship contribution statement

Taeseok Oh: Writing – original draft, Visualization, Validation, Investigation, Formal analysis, Data curation. **Rak Hyeon Choi:** Writing – original draft, Visualization, Validation, Investigation, Formal analysis, Data curation. **Hye Ryung Byon:** Writing – review & editing, Supervision, Resources, Project administration, Funding acquisition, Conceptualization. **Myungeun Seo:** Writing – review & editing, Supervision, Resources, Project administration, Funding acquisition.

Declaration of competing interest

The authors declare that they have no known competing financial interests or personal relationships that could have appeared to influence the work reported in this paper.

Acknowledgements

T. O. and R. H. C. contributed equally to this work. This work was supported by the National Research Foundation of Korea (NRF) grants funded by the Korea government (MSIT) (2023R1A2C2005705, RS-2024-00405261, RS2024-00435493, and RS-2021-NR060082).

Supplementary materials

Supplementary material associated with this article can be found, in the online version, at [doi:10.1016/j.ensm.2025.104364](https://doi.org/10.1016/j.ensm.2025.104364).

References

- [1] W. Xu, J. Wang, F. Ding, X. Chen, E. Nasybulin, Y. Zhang, J.-G. Zhang, Lithium metal anodes for rechargeable batteries, *Energy Env. Sci* 7 (2014) 513–537, <https://doi.org/10.1039/C3EE40795K>.
- [2] B. Liu, J.-G. Zhang, W. Xu, Advancing lithium metal batteries, *Joule* 2 (5) (2018) 833–845, <https://doi.org/10.1016/j.joule.2018.03.008>.
- [3] J. Jeong, J. Chun, W.-G. Lim, W.B. Kim, C. Jo, J. Lee, Mesoporous carbon host material for stable lithium metal anode, *Nanoscale* 12 (2020) 11818–11824, <https://doi.org/10.1039/D0NR02258F>.
- [4] P. Albertus, S. Babinec, S. Litzelman, A. Newman, Status and challenges in enabling the lithium metal electrode for high-energy and low-cost rechargeable batteries, *Nat. Energy* 3 (2017) 16–21, <https://doi.org/10.1038/s41560-022-01077-8>.
- [5] K.J. Harry, D.T. Hallinan, D.Y. Parkinson, A.A. MacDowell, N.P. Balsara, Detection of subsurface structures underneath dendrites formed on cycled lithium metal electrodes, *Nat. Mater.* 13 (2014) 69–73, <https://doi.org/10.1038/nmat3793>.
- [6] C. Wei, L. Tan, Y. Tao, Y. An, Y. Tian, H. Jiang, J. Feng, Y. Qian, Interfacial passivation by room-temperature liquid metal enabling stable 5 V-class lithium-metal batteries in commercial carbonate-based electrolyte, *Energy Storage Mater.* 34 (2021) 12–21, <https://doi.org/10.1016/j.ensm.2020.09.006>.
- [7] C. Wei, Y. Wang, Y. Zhang, L. Tan, Y. Qian, Y. Tao, S. Xiong, J. Feng, Flexible and stable 3D lithium metal anodes based on self-standing MXene/COF frameworks for high-performance lithium-sulfur batteries, *Nano Res.* 14 (10) (2021) 3576–3584, <https://doi.org/10.1007/s12274-021-3433-9>.
- [8] D.-H. Liu, Z. Bai, M. Li, A. Yu, D. Luo, W. Liu, L. Yang, J. Lu, K. Amine, Z. Chen, Developing high safety Li-metal anodes for future high-energy Li-metal batteries:

- strategies and perspectives, *Chem. Soc. Rev.* 49 (2020) 5407–5445, <https://doi.org/10.1039/c9cs00636b>.
- [9] F. Ding, W. Xu, G.L. Graff, J. Zhang, M.L. Sushko, X. Chen, Y. Shao, M. H. Engelhard, Z. Nie, J. Xiao, X. Liu, P.V. Sushko, J. Liu, J.-G. Zhang, Dendrite-free lithium deposition via self-healing electrostatic shield mechanism, *J. Am. Chem. Soc.* 135 (11) (2013) 4450–4456, <https://doi.org/10.1021/ja312241y>.
 - [10] Y. Liu, D. Lin, Z. Liang, J. Zhao, K. Yan, Y. Cui, Lithium-coated polymeric matrix as a minimum volume-change and dendrite-free lithium metal anode, *Nat. Commun.* 7 (2016) 10992, <https://doi.org/10.1038/ncomms10992>.
 - [11] B. Liu, Y. Jia, C. Yuan, L. Wang, X. Gao, S. Yin, J. Xu, Safety issues and mechanisms of lithium-ion battery cell upon mechanical abusive loading: A review, *Energy Storage Mater.* 24 (2020) 85–112, <https://doi.org/10.1016/j.ensm.2019.06.036>.
 - [12] H. Wu, Z. Xie, Y. Wang, P. Zhang, L. Sun, C. Lu, Z. Ma, A constitutive model coupling irradiation with twophase lithiation for lithium-ion battery electrodes, *Phil. Mag.* 99 (8) (2019) 992–1013, <https://doi.org/10.1080/14786435.2019.1569767>.
 - [13] X. Duan, W. Jiang, Y. Zou, W. Lei, Z. Ma, A coupled electrochemical–thermal–mechanical model for spiral-wound Li-ion batteries, *J. Mater. Sci.* 53 (2018) 10987–11001, <https://doi.org/10.1007/s10853-018-2365-6>.
 - [14] P. Bai, J. Li, F.R. Brushett, M.Z. Bazant, Transition of lithium growth mechanisms in liquid electrolytes, *Energy Env. Sci.* 9 (2016) 3221–3229, <https://doi.org/10.1039/C6EE01674J>.
 - [15] Z. Hao, Y. Wu, Q. Zhao, J. Tang, Q. Zhang, X. Ke, J. Liu, Y. Jin, H. Wang, Functional separators regulating ion transport enabled by metal-organic frameworks for dendrite-free lithium metal anodes, *Adv. Funct. Mater.* 31 (33) (2021) 2102938, <https://doi.org/10.1002/adfm.202102938>.
 - [16] X. Han, T. Wu, L. Gu, M. Chen, J. Song, D. Tian, J. Chen, Li-MOF-based ions regulator enabling fast-charging and dendrite-free lithium metal anode, *Chin. Chem. Lett.* 34 (2) (2023) 107594, <https://doi.org/10.1016/j.ccl.2022.06.017>.
 - [17] C. Kim, W. Jeong, H.R. Shin, K.-N. Jung, J.-W. Lee, Robust metal–organic framework monoliths for long-term cycling lithium metal batteries, *J. Mater. Chem. A* 12 (2024) 10686–10694, <https://doi.org/10.1039/d4ta00488d>.
 - [18] K. Yang, Sheng L, D. Zhu, X. Wang, Z. Tang, J. Chen, R. Chen, J. Deng, J. Wang, Y. Tang, X. He, H. Xu, Uniform poly(vinyl ethylene carbonate) based metal-organic framework separator for smooth lithium-ion electrodeposition, *J. Power Source* 624 (2024) 235553, <https://doi.org/10.1016/j.jpowsour.2024.235553>.
 - [19] S. Jalees, A. Hussain, R. Iqbal, W. Raza, A. Ahmad, A. Saleem, M.K. Majeed, M. Faheem, N. Ahmad, L.N.U. Rehman, S. Rauf, H. Li, Functional PBI membrane based on polyimide covalent organic framework for durable lithium metal battery, *J. Energy Storage* 101 (2024) 113985, <https://doi.org/10.1016/j.est.2024.113985>.
 - [20] J. Zhong, Y. Tong, L. Guo, A. Zhang, Q. Xu, Y. Qin, Cationic covalent organic framework-modified polypropylene separator for high-performance lithium metal batteries, *ACS Appl. Mater. Interfaces* 16 (41) (2024) 56106–56115, <https://doi.org/10.1021/acsami.4c11328>.
 - [21] J.Y. Song, Y.Y. Wang, C.C. Wan, Review of gel-type polymer electrolytes for lithium-ion batteries, *J. Power. Source* 77 (1999) 183–197, [https://doi.org/10.1016/S0378-7753\(98\)00193-1](https://doi.org/10.1016/S0378-7753(98)00193-1).
 - [22] K. Deng, Q. Zeng, D. Wang, Z. Liu, Z. Qiu, Y. Zhang, M. Xiao, Y. Meng, Single-ion conducting gel polymer electrolytes: design, preparation and application, *J. Mater. Chem. A* 8 (2020) 1557–1577, <https://doi.org/10.1039/C9TA11178F>.
 - [23] K. Deng, Q. Zeng, D. Wang, Z. Liu, G. Wang, Z. Qiu, Y. Zhang, M. Xiao, Y. Meng, Nonflammable organic electrolytes for high-safety lithium ion batteries, *Energy Storage Mater.* 32 (2020) 425–447, <https://doi.org/10.1016/j.ensm.2020.07.018>.
 - [24] Q. Zhang, Y. Wu, M. Li, N. Wang, K. Deng, Active fluorobenzene diluent regulated tetraglyme electrolyte enabling high-performance Li metal batteries, *Energy Storage Mater.* 74 (2025) 103940, <https://doi.org/10.1016/j.ensm.2024.103940>.
 - [25] R. He, K. Deng, D. Mo, X. Guan, Y. Hu, K. Yang, Z. Yan, H. Xie, Active diluent-anion synergy strategy regulating nonflammable electrolytes for high-efficiency Li metal batteries, *Angew. Chem. Int. Ed.* 63 (2024) e202317176, <https://doi.org/10.1002/anie.202317176>.
 - [26] Y. Cao, H. Wu, G. Li, C. Liu, L. Cao, Y. Zhang, W. Bao, H. Wang, Y. Yao, S. Liu, F. Pan, Z. Jiang, J. Sun, Ion selective covalent organic framework enabling enhanced electrochemical performance of lithium–sulfur batteries, *Nano Lett.* 21 (7) (2021) 2997–3006, <https://doi.org/10.1021/acs.nanolett.1c00163>.
 - [27] K. Jeong, S. Park, G.Y. Jung, S.H. Kim, Y.-H. Lee, S.K. Kwak, S.-Y. Lee, Solvent-free, single lithium-ion conducting covalent organic frameworks, *J. Am. Chem. Soc.* 141 (14) (2019) 5880–5885, <https://doi.org/10.1021/jacs.9b00543>.
 - [28] R.H. Choi, J. So, Y. Kim, D. Lee, H.R. Byon, Li⁺ conduction of soft-base anion-immobilized covalent organic frameworks for all-solid-state lithium–metal batteries, *ACS Energy Lett.* 9 (11) (2024) 5341–5348, <https://doi.org/10.1021/acscenergylett.4c01941>.
 - [29] Q. Ai, Q. Fang, J. Liang, X. Xu, T. Zhai, G. Gao, H. Gao, G. Han, L. Ci, J. Lou, Lithium-conducting covalent-organic-frameworks as artificial solid-electrolyte-interphase on silicon anode for high performance lithium ion batteries, *Nano Energy* 72 (2020) 104657, <https://doi.org/10.1016/j.nanoen.2020.104657>.
 - [30] D. Guo, L. Mu, F. Lin, G. Liu, Mesoporous polyimide thin films as dendrite-suppressing separators for lithium–metal batteries, *ACS Nano* 18 (1) (2024) 155–163, <https://doi.org/10.1021/acsnano.3c04159>.
 - [31] Y.-k. Ahn, J. Park, D. Shin, S. Cho, S.Y. Park, H. Kim, Y. Piao, J. Yoo, Y.S. Kim, Enhanced electrochemical capabilities of lithium ion batteries by structurally ideal AAO separator, *J. Mater. Chem. A* 3 (2015) 10715–10719, <https://doi.org/10.1039/c5ta01892g>.
 - [32] J. Chen, S. Wang, L. Ding, Y. Jiang, H. Wang, Performance of through-hole anodic aluminum oxide membrane as a separator for lithium-ion battery, *J. Membr. Sci.* 461 (2014) 22–27, <https://doi.org/10.1016/j.memsci.2014.03.005>.
 - [33] M. Seo, M.A. Hillmyer, Reticulated nanoporous polymers by controlled polymerization-induced microphase separation, *Science* (1979) 336 (6087) (2012) 1422–1425, <https://doi.org/10.1126/science.1221383>.
 - [34] T. Oh, S. Cho, C. Yoo, W. Yeo, J. Oh, M. Seo, Polymerization-induced microphase separation of a polymerization mixture into nanostructured block polymer materials, *Prog. Polym. Sci.* 145 (2023) 101738, <https://doi.org/10.1016/j.progpolymsci.2023.101738>.
 - [35] K. Lee, N. Corrigan, C. Boyer, Polymerization induced microphase separation for the fabrication of nanostructured materials, *Angew. Chem. Int. Ed.* 62 (2023) e202307329, <https://doi.org/10.1002/anie.202307329>.
 - [36] K.I. Anigbaoso, J. Bitenc, V. Pellerin, M. Save, A. Bousquet, L. Rubat, *In situ* fabrication of quasi-solid polymer electrolytes for lithium metal battery via photopolymerization-induced microphase separation, *ACS Appl. Mater. Interfaces* 17 (2) (2025) 3876–3886, <https://doi.org/10.1021/acsami.4c15921>.
 - [37] C. Jeon, J.J. Han, M. Seo, Control of ion transport in sulfonated mesoporous polymer membranes, *ACS Appl. Mater. Interfaces* 10 (47) (2018) 40854–40862, <https://doi.org/10.1021/acsami.8b14712>.
 - [38] C. Jeon, Choi C, H.-T. Kim, M. Seo, Achieving fast proton transport and high vanadium ion rejection with uniformly mesoporous composite membranes for high-efficiency vanadium redox flow batteries, *ACS Appl. Energy Mater.* 3 (6) (2020) 5874–5881, <https://doi.org/10.1021/acsaem.0c00804>.
 - [39] J. Park, S.A. Saba, M.A. Hillmyer, D.-C. Kang, M. Seo, Effect of homopolymer in polymerization-induced microphase separation process, *Polym. (Guildf)* 126 (2017) 338–351, <https://doi.org/10.1016/j.polymer.2017.04.046>.
 - [40] V. Muralidharan, C.-Y. Hui, Stability of nanoporous materials, *Macromol. Rapid. Commun.* 25 (16) (2004) 1487–1490, <https://doi.org/10.1002/marc.200400190>.
 - [41] K.A. Cavicchi, A.S. Zalusky, M.A. Hillmyer, T.P. Lodge, An ordered nanoporous monolith from an elastomeric crosslinked block copolymer precursor, *Macromol. Rapid. Commun.* 25 (6) (2004) 704–709, <https://doi.org/10.1002/marc.200300245>.
 - [42] K.D. Fong, J. Self, K.M. Diederichsen, B.M. Wood, B.D. McCloskey, Persson K.A, Ion transport and the true transference number in nonaqueous polyelectrolyte solutions for lithium ion batteries, *ACS Cent. Sci.* 5 (7) (2019) 1250–1260, <https://doi.org/10.1021/acscentsci.9b00406>.
 - [43] J. Yang, C.-Y. Wang, C.-C. Wang, K.-H. Chen, C.-Y. Mou, H.-L. Wu, Advanced nanoporous separators for stable lithium metal electrodeposition at ultra-high current densities in liquid electrolytes, *J. Mater. Chem. A* 8 (10) (2020) 5095–5104, <https://doi.org/10.1039/C9TA13778E>.